Dynamics of phase transformations and microstructure evolution in carbon–manganese steel arc welds using time-resolved synchrotron X-ray diffraction

Joe Wong, Thorsten Ressler and John W. Elmer

research papers

Dynamics of phase transformations and microstructure evolution in carbon–manganese steel arc welds using time-resolved synchrotron X-ray diffraction

Joe Wong,* Thorsten Ressler† and John W. Elmer

Lawrence Livermore National Laboratory, University of California, PO Box 808, Livermore, CA 94551, USA. E-mail: wong10@llnl.gov

Phase transformations that occur in both the heat-affected zone (HAZ) and the fusion zone (FZ) of a carbon–manganese steel spot weld have been investigated using time-resolved X-ray diffraction (TRXRD) with time resolutions down to 50 ms. It is found that in both zones the γ(f.c.c.) $\rightarrow$ α(b.c.c.) transformation on cooling is twice as fast as the forward transformation of $\alpha \rightarrow \gamma$ on heating. Profile analysis of the major Bragg reflections recorded in the TRXRD patterns reveals similarities and differences in the microstructural evolution with time in the HAZ and in the FZ. The latter undergoes melting and solidification in addition to solid-state transformations. With increasing temperature, the (110) d-spacing of the α phase prior to and during the $\alpha \rightarrow \gamma$ transformation and the (111) d-spacing of the γ phase just after the same transformation exhibit a decrease. The observed (and unusual) lattice contraction with temperature rise may be attributed to chemical effects, such as carbide precipitation in the α matrix, and/or mechanical effects due to stress relief. In the FZ, the γ-Fe that forms has a preferential (200) texture on solidification of the liquid, whereas, on cooling in the HAZ, the γ-Fe retains largely a (111) texture that is induced in the $\alpha \rightarrow \gamma$ transformation on heating. On cooling in the HAZ, the width of the γ(111) reflection increases initially, which is indicative of microstrain developing in the f.c.c. lattice, but decreases as expected, with a reduction of thermal disorder, on further cooling until the completion of the $\gamma \rightarrow \alpha$ transformation. In the FZ, however, the microstrain in the γ phase increases steadily on solidification and more rapidly for the duration of the $\gamma \rightarrow \alpha$ transformation on further cooling. The final microstructure of the FZ is likely to consist of a single α phase dispersed in two morphological entities, whereas in the HAZ the α phase persists in one morphological entity in the final microstructure.

1. Introduction

Real-time studies of dynamical processes under severe temperature or pressure conditions often pose a challenge to experimentalists. During fusion welding, high-intensity sources are employed to create steep thermal gradients that rapidly heat and cool materials to and from their melting point. This rapid thermal cycling induces solid-state transformations both on heating and on cooling as well as melting and solidification in those regions of the weld where the liquidus temperature has been exceeded. In the heat-affected zone (HAZ) of fusion welds, microstructural gradients are created by processes such as grain growth, recrystallization, phase changes, annealing and tempering (Grong, 1994; Easterling, 1983; Ashby & Easterling, 1982; Ion et al., 1984). In steels, these transformations result in the formation of different microstructural subregions that are referred to as the coarse-grain region, the fine-grain region and the partially transformed region of the HAZ (Grong, 1994; Easterling, 1983; Ashby & Easterling, 1982; Ion et al., 1984). The presence of these various microstructural regions is known in a qualitative sense. However, their exact size, location and temporal development have not been determined and well understood until recently because of a lack of appropriate experimental methods for in situ determination of phase transformations in fusion welds (Wong et al., 1994, 1997; Elmer et al., 1996, 1998, 2000, 2001; Ressler et al., 1998; Palmer et al., 2001). This lack of information has hindered both our basic understanding of microstructural evolution in steel welds and efforts to develop comprehensive models for the prediction of the HAZ microstructure.

Experimental measurements of phase-transformation dynamics in welds are difficult to perform because of the highly non-isothermal and transient heating conditions that exist during welding. In the absence of specific kinetic data under true welding conditions, isothermal time–temperature-transformation (TTT) and continuous-cooling-transformation (CCT) diagrams have been developed. These diagrams are available for many ferrous alloys (Vander Voort, 1991; Harrison & Farrar, 1989) and are often used to approximate the behavior of phase transformations that occur during cooling of the HAZ (Easterling, 1983). However, the prediction of weld microstructures from CCT diagrams requires many assumptions in order to deal with the non-isothermal and non-uniform cooling conditions of welds (Easterling, 1983). Furthermore, these diagrams represent the *cooling* but not the *heating* portions of the HAZ, and there is no generally accepted method for validating how well these diagrams predict actual HAZ behavior.

Modeling the phase transformations that occur in the HAZ during welding requires a good understanding of both the temperature cycles that occur during welding and the kinetics of the phase transformations. Numerical modeling of the weld temperatures has advanced considerably in the past few years and is now being used by welding metallurgists to calculate the size and shape of the fusion zone (FZ) in carbon steels (Yang & DebRoy, 1997, 1999; Mundra et al., 1997) and other alloys such as titanium (Yang et al., 2000). These models provide semi-quantitative, but very useful, information about transient three-dimensional temperature distribution around the weld, thus allowing the spatial distribution of peak temperatures, heating rates and cooling rates in the HAZ to be determined. However, without corresponding transformation kinetics and phase dynamics, microstructural evolution in the weld HAZ cannot be predicted accurately.

In this work, we have applied a refined version of the time-resolved diffraction technique (Wong et al., 1990; Larson et al., 1993), which was originally developed for chemical-dynamics studies of fast high-temperature solid combustion reactions, in order to investigate the phase-transformation dynamics in both the HAZ and the FZ of a simple C–Mn steel spot weld. In particular, the $\alpha \rightarrow \gamma$ transformation on heating and the reverse $\gamma \rightarrow \alpha$ transformation on cooling have been examined in detail. We have used quantitative profile analysis of the major Bragg reflections recorded in the TRXRD patterns as a function of time during welding, with time resolutions down to 50 ms. The results yield new insight into the microstructural evolution in both the HAZ and the FZ and should provide the much needed experimental inputs for realistic modeling.

2. Experimental

2.1. Carbon–manganese steel (AISI 1005 steel)

The starting C–Mn steel was in the form of 10.8 cm-diameter forged bar stock. Cylindrical welding samples were machined from the as-received material into 10.15 cm-diameter bars of length 11.40 cm. The final cylindrical samples had a surface roughness of 1.6 μm r.m.s. and were circular in diameter to within 10 μm. The composition was assayed using a combination of combustion analysis, for O, C, N and H, and inductively coupled plasma analysis for the remaining elements. The results show the following elemental constitution in weight percent: C 0.05%; Mn 0.31%; Si 0.18%; Ni 0.11%; Cr 0.10%; P 0.009%; Cu 0.08%; S 0.005%; Al < 0.005%; Nb < 0.005%; Mo < 0.005%; Ti < 0.005%; and V < 0.005%. The phases present in the HAZ of a moving fusion weld of this material under steady-state conditions have recently been mapped in detail using a spatially resolved diffraction method (Elmer et al., 2001).

2.2. Welding

Gas tungsten arc spot welds were made on the steel bars using a 225 A constant direct-current welding power supply with electrode negative polarity. The welding electrode was made of tungsten–2% thorium, measured 4.7 mm in diameter and was straight ground with a 90° included angle taper. The average power was maintained at 2.1 kW (120 A, 17.5 V) for all of the welds, and current pulsing was used to help minimize the side-to-side motion of the liquid weld pool. The pulsing parameters used were 145 A maximum current, 101.5 A background current and 50% peak current on time at 300 pulses per second. Welding was performed in an environmentally controlled chamber in order to optimize the signal-to-noise ratios in the diffraction data by obviating oxidation of the steel bar during welding and minimizing air absorption of the X-ray beam.

Prior to welding, the vacuum chamber was evacuated to 60 mtorr with a mechanical roughing pump and then back-filled with ultra-high-purity (99.999%) helium gas. This gas was also flowed through the torch during welding to prevent oxidation in the weld region and to cool the torch. A second He gas stream was blown across the weld pool to obviate soot accumulation in the weld region probed by the X-ray beam. The chamber contained two 50 mm-diameter ports. The first port was sealed with a 0.125 mm-thick mylar window, which allowed the X-rays to enter the chamber. The second port was sealed with a KBr crystal and was used to video record the weld with an IR camera (Inframetrics, Model 600) with a 0.46 m focal length lens and a 40 × 25 mm field of view. The IR camera provided real-time visual monitoring of the welding process. The welding-diffraction chamber has been described elsewhere (Elmer et al., 1998; Ressler et al., 1998).

The welds were made with the torch perpendicular to the surface of the bar, while the steel bar was held stationary below the fixed electrode during welding and X-ray measurement. The total arc-on time varied between 15 and 25 s, during which X-ray diffraction patterns were recorded at a predetermined position about the weld as a function of time, with temporal resolution in the range 50–200 ms. This configuration together with a nominal power input of 2.1 kV yielded a circular spot weld with a ∼8.5 ± 0.5 mm-diameter fusion zone on the surface of the steel bar.

2.3. Time-resolved X-ray diffraction

TRXRD measurements were performed on the 31-pole wiggler beamline, BL 10–2 (Karpenko et al., 1989), at Stanford Synchrotron Radiation Laboratory (SSRL) with SPEAR (Stanford Positron–Electron Accumulation Ring) operating at an electron energy of 3.0 GeV and an injection current of ∼100 mA. The synchrotron white beam emerging from the 31-pole wiggler was first focused by a toroidal mirror to the source size of ∼1 mm vertical × 2 mm horizontal and monochromated downstream with a double Si(111) crystal. The focused monochromatic beam was then passed through a tungsten pinhole to render a submillimeter beam on the sample at an incident angle of ∼25°. Using an ion chamber immediately downstream from the pinhole, we determined the beam flux on the sample to be ∼10^{10}–10^{11} photons s^{-1} for pinholes ranging from 260 to 730 μm. A photon energy of 12.0 keV (λ = 0.1033 nm) was chosen to maximize the number of Bragg peaks in a selected 2θ window in order (i) to facilitate phase identification and (ii) to be far enough in energy above the Fe-edge to minimize the background contribution due to Fe K-fluorescence from the sample [Fe K-edge at 7.112 keV (Bearden & Burr, 1967)]. For higher resolution in 2θ, we used a 7 keV photon beam (λ = 0.1771 nm), the energy of which is below the Fe K-edge.

TRXRD patterns were recorded using a 50 mm-long 2048-element position-sensitive silicon photodiode array detector. The array was mounted on a Peltier effect cooler, which in turn was water cooled. This detector was placed ∼10 cm behind the weld to cover a 2θ range from 24° to 54°. This range of 2θ was optimized at 12 keV to contain a total of six diffraction peaks: three from the body-centered cubic (b.c.c.) phases (α-Fe or δ-Fe) and three from the face-centered cubic (f.c.c.) phase (γ-Fe). The detector together with the associated ST121 data acquisition system was manufactured by Princeton Instruments (now Roper Scientific) (ST121 Detector and Controller Manual, 1996) and was used to store and display the X-ray diffraction data in real time.

The TRXRD procedure consists of first positioning the X-ray beam at a predetermined location in the FZ or HAZ using the electrode position as the center of the liquid pool. After an inert ambient was established with pumping and He back fill, an arc was struck to establish a spot weld. Diffraction patterns were collected within a few seconds at a preset time interval (resolution), in order to record the phase transformations in a predetermined heating (arc on) and cooling (arc off) cycle. Preliminary results indicated that a time resolution of 100 ms in conjunction with a 260 μm pinhole used for phase mapping of the same system (Elmer et al., 2001) was adequate to capture the α → γ phase transformation on heating and the γ → α transformation on cooling in the HAZ. For phase transformations in the FZ, where (a) the thermal gradients are much higher and (b) larger grains are present as a result of solidification, a 730 μm pinhole was used to enhance the time resolution to 50 ms and at the same time to incorporate more grains into the diffraction beam. The ultimate time resolution of the diode array is 8 ms, which is determined by a read-out time of 4 μs for each of the 2048 pixels in the array (ST121 Detector and Controller Manual, 1996).

2.4. Data analysis

The X-ray diffraction data were analyzed using the WinXAS software package (Ressler, 1997). Conversion from detector pixel number to 2θ angle (in °) was performed using the calibration curve

$$2\theta = 23.950 + 0.015 \times \text{pixel number}, \qquad (1)$$

which was derived using the (110), (200), (211) and (220) diffraction peaks of a pure niobium foil laid over the surface of the steel-bar sample at room temperature. The 2θ values of the observed hkl peaks were calculated (with PowerCell[1]) from the known cell constant

---

[1] Version 1.2. W. Kraus & G. Nolze, Federal Institute for Materials Research & Testing, Rudower Chaussee 5, 12489 Berlin, Germany. A free version may be obtained from gert.nolze@Bam.de.

(0.33002 nm; Wychoff, 1963) of b.c.c. Nb at room temperature. Given a detector resolution of 1.5 diode (pixel) or better (*ST121 Detector and Controller Manua*l, 1996), the angular resolution of the present TRXRD setup is 0.0225° in 2θ or better. Single or multiple diffraction peaks in the TRXRD data were fitted with a sum of one or more Gaussian profile functions and a linear background *via* a standard least-squares refinement procedure. Because of the limited number of data points in multiple-peak diffraction lines, the FWHMs of the respective Gaussian functions were refined to vary identically. Multiple-scan data in each TRXRD file were analyzed in a serial procedure employing the macro capabilities of *WinXAS*.

3. Results

3.1. TRXRD patterns

3.1.1. Phase transformation in the HAZ. Having experimentally determined the weld-pool diameter to be ∼8.5 mm with the power input and welding configuration described in §2, we positioned the X-ray beam at spots 5 mm and 3 mm from the electrode in order to follow crystallographically the phase transformations in the HAZ and FZ using TRXRD.

Fig. 1(*a*) shows a series of TRXRD patterns recorded in the HAZ at a location 5 mm away from the center of the liquid pool. The data were recorded with a 260 µm pinhole at 12 keV and a time resolution of 100 ms. For clarity, only every 15th of the 600 TRXRD patterns were shown in the pseudo three-dimensional plot given in Fig. 1(*a*). As the arc was turned on and off, diffraction patterns were continuously recorded in order to follow the annealing and phase transformation in real time in both the heating and the cooling cycles. Frame-by-frame qualitative analysis of the TRXRD data yielded a real-time sequence of events in the HAZ, which is schematically shown in Fig. 1(*b*). In this plot, *t* = 0 corresponds to the start of the TRXRD measurement at room temperature. At *t* = 1.0 s, the arc was turned on and heating began. Annealing of the b.c.c. α phase took place in the next 7.1 s. At *t* = 8.1 s, the f.c.c. γ phase first appeared, marking the start of the α → γ transformation. This transformation was completed within 1.1 s, and at *t* = 9.2 s only γ-Fe existed. This phase persisted for the whole time that the arc was on.

At *t* = 25.0 s, the arc was turned off. The γ phase cooled, and at *t* = 25.7 s the first back-transformed α-Fe was observed, which signified the start of the reverse γ → α transformation. At *t* = 26.1 s, all γ-Fe disappeared, denoting completion of the γ → α transformation. From then, only α-Fe existed, which cooled with time. Note that the α → γ transformation upon heating takes about twice as long as the γ → α transformation upon cooling.

3.1.2. Phase transformation in the FZ. In Fig. 2(*a*), the TRXRD patterns recorded in the FZ at a position 3 mm away from the center of the liquid pool are shown. The data were recorded through a 730 µm pinhole with a time resolution of 50 ms at 12 keV of photon energy. Again, for clarity, only every 15th of the 600 TRXRD patterns were shown in Fig. 2(*a*). Frame-by-frame qualitative analysis of the TRXRD data yielded the real-time sequence of events in the FZ that are schematically shown in Fig. 2(*b*). Again, *t* = 0 corresponds to the start of the TRXRD measurement at room temperature. At *t* = 1.20 s, the arc was turned on and heating began. Annealing of the b.c.c. α phase took place in the next 1.30 s, which was much sooner than in the HAZ (7.1 s). At *t* = 2.50 s, the f.c.c. γ phase first appeared, marking the start of the α → γ transformation in the FZ on heating. This transformation, which was similar to that in the HAZ, was completed within 1.10 s, and at *t* = 3.60 only γ-Fe existed. This phase persisted for 10.50 s. At *t* = 14.10 s all of the γ phase disappeared and

no diffraction peaks were observed, which signifies that the system melted.

At *t* = 17.35 s, the arc was turned off. The γ phase reappeared and cooled. At *t* = 18.10 s, the first back-transformed α-Fe was observed, signifying the start of the γ → α transformation.

At *t* = 18.65 s, all γ-Fe disappeared, denoting the completion of the γ → α transformation. From then, only α-Fe existed, which cooled with time. Note that, again, the α → γ transformation upon heating takes about twice as long as the γ → α transformation upon cooling.

4. Discussion

4.1. Phase equilibria

Pure iron at normal pressure exists in both the b.c.c. and the f.c.c. crystal forms (Honeycomb, 1982): α-Fe and δ-Fe are both b.c.c., while γ-Fe is f.c.c. The α phase is stable at room temperature and completely transforms to γ-Fe at 1183 K. At 1663 K the γ-Fe begins to transform back to a b.c.c. phase (now called δ-Fe). The δ-Fe then remains stable up to the melting point at 1809 K.

The AISI 1005 C–Mn steel used in this investigation is similar to pure iron in that it undergoes each of these phase transformations, but the steel contains, in addition, carbides in the microstructure at lower temperatures (Honeycomb, 1982). One of these carbides, cementite, Fe_3C, transforms to a mixture of α-Fe (ferrite) and γ-Fe
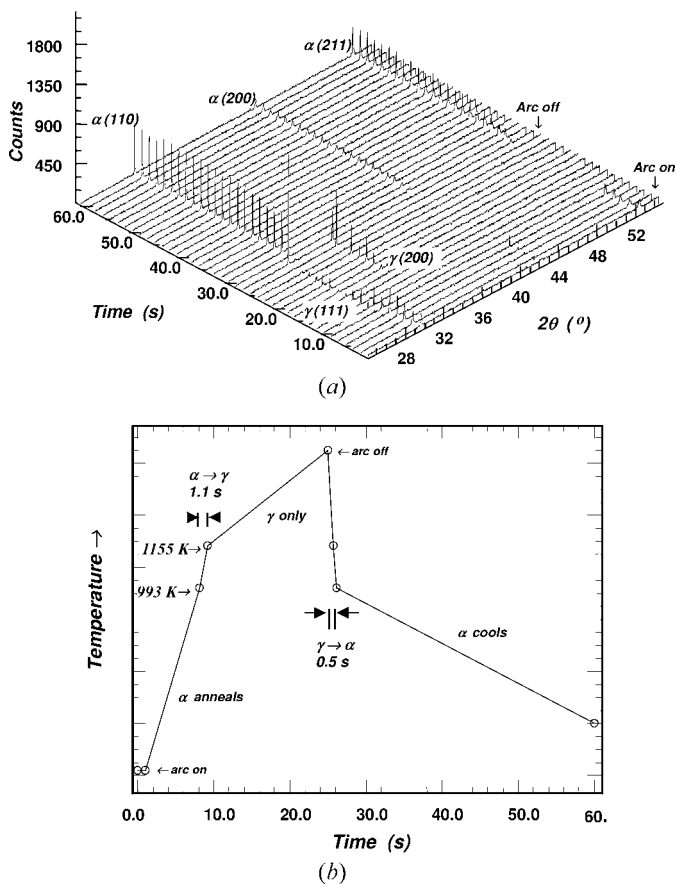

(*a*)

(*b*)

Figure 1
(*a*) TRXRD patterns recorded in the HAZ of the carbon–manganese steel spot weld at a position 5 mm from the weld center. The parameters are 12 keV, 260 µm pinhole and 100 ms time resolution. For clarity, only every 15th of the 600 frames is plotted. (*b*) A temperature–time schematic depicting the recorded TRXRD events given in (*a*). The scale for the temperature axis is discussed in the text.

(austenite) at 1000 K, which is called the A1 temperature in Fe–C alloys. Manganese, silicon and trace impurities present in the 1005 steel further alter the phase-transformation temperatures, and these changes can be calculated from thermodynamic relationships. The phase-transformation temperatures for the particular AISI 1005 steel used in this investigation have been calculated by Babu (2000) using *Thermocalc* (Sundman *et al.*, 1985). These calculations took into consideration the effects of Fe, C, Si, Mn, Ni and Cr on the cementite, α-ferrite, γ-austenite, δ-ferrite and liquid-phase fields. The results of the phase-boundary temperatures calculated for this multicomponent alloy are shown in a pseudo-binary diagram in Fig. 3. The first transformation on heating begins at 993 K as the cementite dissolves to yield a mixture of α-Fe and γ-Fe. The α-Fe disappears at 1155 K and the $\alpha \to \gamma$ transformation is complete. These two temperatures are labeled in Figs. 1(*b*) and 2(*b*). Above 1155 K, γ-Fe remains as the only solid phase up to 1705 K, where δ-Fe first appears. The δ-Fe coexists with γ-Fe up to 1735 K, where γ-Fe disappears, which leaves δ-Fe as the only solid phase up to the melting point at 1802 K.

Note that the δ-Fe phase was not observed in the TRXRD patterns for the HAZ (Fig. 1) before the arc was turned off, which indicates that at this position (5 mm from the weld center) and these arc-power inputs the temperature did not reach 1705 K. This finding agrees with

the phase mapping results for a moving weld of the same steel (Elmer *et al.*, 2001) under similar arc-power conditions. Furthermore, TRXRD data for the FZ (Fig. 2) also did not show the appearance of the δ-Fe phase, even though the system did pass into the liquid state before the arc was turned off. This point will be discussed later. Next we will elucidate the dynamics of the phase transformation and the associated microstructural evolution in the HAZ and FZ on heating and on cooling, by performing systematic profile analysis on the experimental TRXRD patterns.

4.2. Dynamics of phase transformation in the HAZ

4.2.1. Annealing of α-Fe and the $\alpha \to \gamma$ transformation on heating. The TRXRD data shown in Fig. 1(*a*) for the phase transformations in the HAZ will now be examined in more detail, with profile analysis on a frame-by-frame basis. Fig. 4 is a frame-by-frame plot of the phases participating in the transformation. The $\alpha \to \gamma$ transformation began at $t = 8.1$ s, as shown clearly by the first appearance of the γ phase. At $t = 9.2$ s α-Fe disappeared, which indicates the completion of the $\alpha \to \gamma$ transformation. According to the calculated phase diagram given in Fig. 3 and assuming no superheating, the temperatures at the start and end of this transformation should be 993 K and 1155 K. From Fig. 4, there are 11 frames of coexistence of the α and γ phases. Since the time resolution of each frame is 0.1 s, the total time of the $\alpha \to \gamma$ transformation is 1.1 s. In order to gain insight into the time-dependent behavior of the α-Fe phase in the HAZ upon heating from room temperature to the $\alpha \to \gamma$ transformation, profile analysis has been performed on the α(110) Bragg peak shown in Fig. 4. The results for the peak height, peak position in 2θ and peak width (FWHM) are plotted in Fig. 5 as a function of time. During the initial heating, in the first 7 s or so, the peak intensity is fairly constant. Beyond that time and prior to the transformation, this reflection undergoes approximately a tenfold fluctuation in peak intensity and exhibits a multipeak feature that can be discerned clearly in the frame-by-frame data in Fig. 4. The increase in peak intensity and multiplet structure in the (110) reflection may be attributed to recrystallization of the base metal to yield a preferential (110) orientation of fine and relatively perfect grains in the microstructure, with a temperature rise near to the start temperature of the $\alpha \to \gamma$ transformation. The multipeak feature persists throughout the
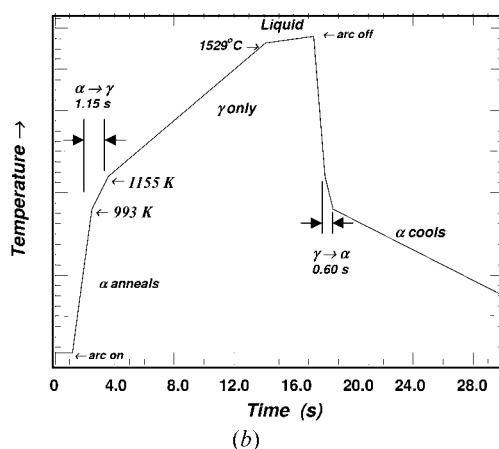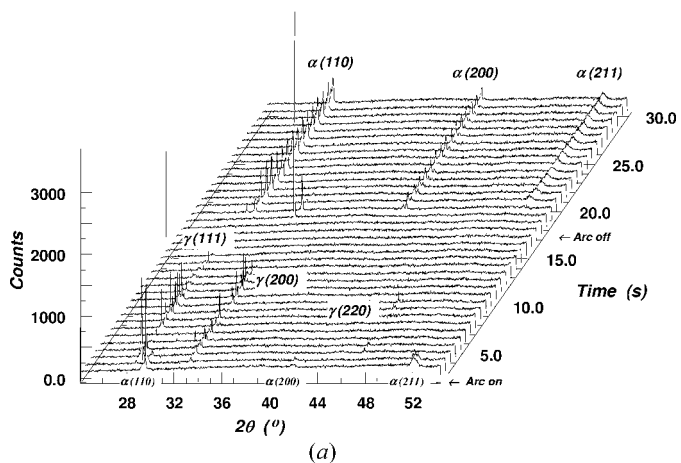

Figure 2
(*a*) TRXRD patterns recorded in the FZ of the manganese–carbon steel weld at a position 3 mm from the weld center. The parameters are 12 keV, 730 µm pinhole and 50 ms time resolution. For clarity, only every 15th of the 600 frames is plotted. (*b*) A temperature–time schematic depicting the recorded TRXRD events given in (*a*). The scale for the temperature axis is discussed in the text.
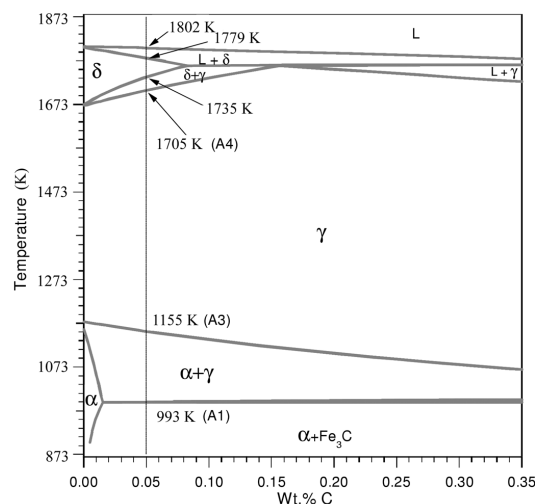

Figure 3
Calculated pseudo-binary Fe–C phase diagram for the AISI steel. The vertical line denotes the carbon content in the samples used in this work.

transformation. On the other hand, the peak position initially decreases in 2θ value along the path PQ in Fig. 5(b), which behavior is indicative of thermal expansion in accordance to Bragg's law. Further
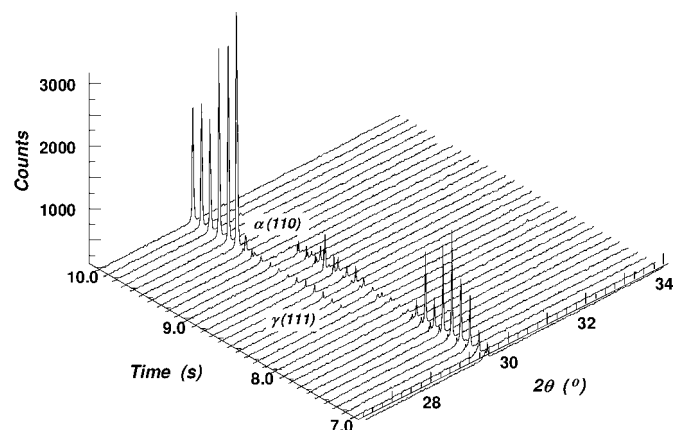

Figure 4
Frame-by-frame plot of the TRXRD patterns in the 2θ region of the $\alpha(110)$ and $\gamma(111)$ peaks from the HAZ on heating over the entire period of the $\alpha \rightarrow \gamma$ transformation. Each frame is 100 ms.
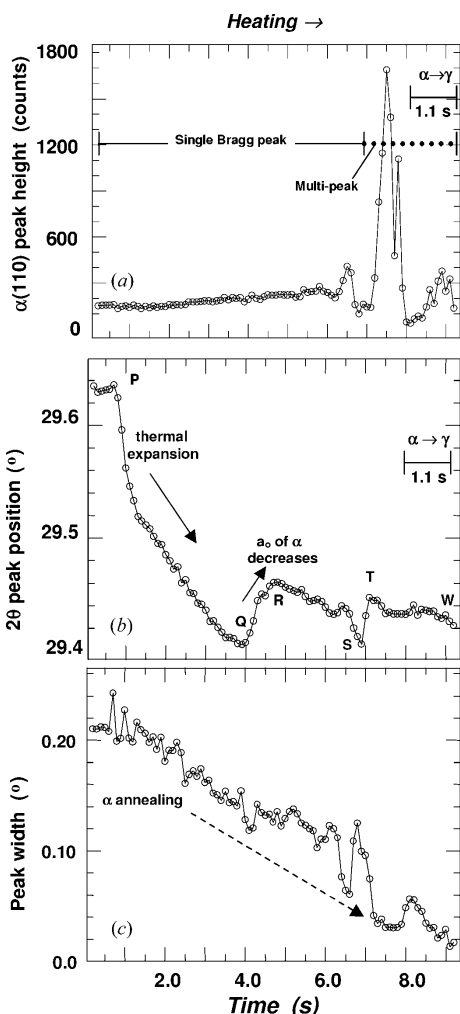

Figure 5
Profile analysis of the $\alpha(110)$ reflection shown in Fig. 4 as recorded in the HAZ on heating: (a) peak height, (b) peak position and (c) peak width (FWHM).

heating along the path QR shows an *unexpected* increase in 2θ position, which corresponds to an apparent decrease in the (110) d-spacing of the Fe b.c.c. lattice. This jump in the 2θ position of the $\alpha(110)$ peak is reproducible at the same location in a duplicate TRXRD experiment using a 540 µm pinhole and a time resolution of 50 ms. From the calibration curve given in (1), the d-spacing contraction was determined to be −0.000334 nm which in turn yields a $\Delta d/d$ ratio of −0.00164. The observed contraction with increasing temperature may arise from chemical effects (carbide precipitation) and/or mechanical effects (relief of process-induced tensile stress), each of which can exceed the normal effects of thermal expansion. Along the path TW, normal thermal expansion of the b.c.c. lattice occurs during the $\alpha \rightarrow \gamma$ transformation from $t = 8.1$ to 9.2 s. In Fig. 5(c), the width of the $\alpha(110)$ reflection is shown to decrease monotonically upon heating until the completion of the transformation, which indicates thermal annealing and the relief of microstrain in the base metal in the heating cycle. Finally, note that the $\alpha(211)$ reflection exhibits identical time dependence in both peak position and peak width to that of the $\alpha(110)$ reflection.

4.2.2. γ-Fe during and after transformation on heating. TRXRD patterns of the γ phase in the HAZ on heating are shown in detail in Fig. 6, from $t = 8.1$ s, when γ-Fe was first observed, to $t = 24$ s, at which time γ-Fe persisted until the arc was turned off. Profile analysis of the $\gamma(111)$ reflection is given in Figs. 7. During the transformation, the peak intensity of $\gamma(111)$ is low. Within 0.5 s of completion of the $\alpha \rightarrow \gamma$ transformation, the γ (111) reflection exhibits a ~20-fold increase in peak intensity; this increase is attributable to texturing associated with recrystallization and grain growth. This stage lasted for just over 1 s. On further heating, the peak intensity drops, thus giving rise to a multipeak feature indicative of multiple domain production in the pure-γ microstructure. The peak position of the $\gamma(111)$ reflection shows a jump in 2θ value along PQ in Fig. 7(b). This increase coincides with the peak intensity increase that is clearly discernible in Fig. 8, which gives a frame-by-frame display of the TRXRD patterns in the time regime in which the newly transformed γ phase exhibits a (111) reflection at a 2θ value corresponding to pixel 315 at $t = 9.2$ s. In the next frame, at $t = 9.3$ s, a new reflection at pixel 319 emerges, and at $t = 9.4$ s this reflection grows at the expense of that at pixel 315. At $t = 9.5$ s the intensity of the new reflection increases approximately tenfold. From the calibration curve given in (1), a four-pixel increase in 2θ value at the $\gamma(111)$ reflection corresponds to a decrease in cell parameter of 0.0043 Å. The jump in 2θ
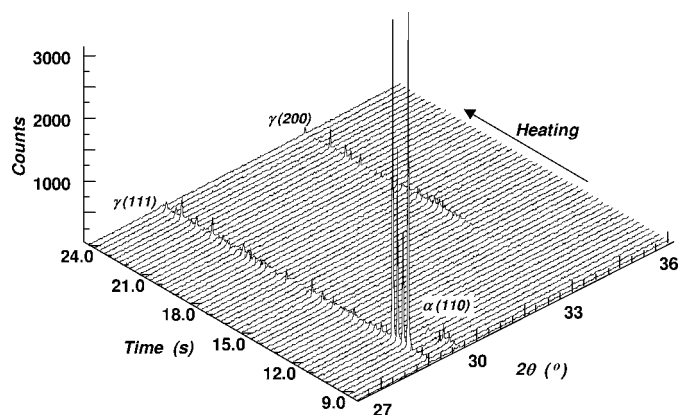

Figure 6
TRXRD patterns of the γ-Fe phase in the HAZ on heating, from the start of the $\alpha \rightarrow \gamma$ transformation to continued heating. For clarity, only every third frame of the 150 frames is plotted.

has been reproduced in three additional experimental runs at the same location of the steel weld. The observed decrease in the (111) d-spacing of the γ phase with increasing temperature is likely to arise from a stress relief in the austenite induced in the phase transformation from a lower-density (b.c.c. at 7.789 gm cc^{-1}) to a slightly higher-density (f.c.c. at 7.862 gm cc^{-1}) phase as estimated from the measured lattice parameters. Finally, in the period $t = 10.5–16$ s, the width of the $\gamma(111)$ reflection increases (Fig. 7c), which indicates dynamic disorder due to the Debye–Waller factor. With further temperature rise in the HAZ beyond $t = 16$ s, annealing of the multidomain γ phase microstructure may give rise to the observed drop in width prior to the arc being turned off.

4.2.3. The $\gamma \rightarrow \alpha$ transformation on cooling. Fig. 9 shows a frame-by-frame plot of the TRXRD data in the time regime of the $\gamma \rightarrow \alpha$ transformation on cooling. At $t = 25.0$ s, the arc was turned off. The existent γ phase cooled and transformed as the temperature was lowered further. At $t = 25.7$ s, α-Fe first appeared. At $t = 26.1$ s, γ-Fe disappeared, marking the completion of the back transformation to the ferrite phase. As can be clearly seen in Fig. 9, there are five frames of coexistence of the γ and α phases. Since the time resolution of each frame is 0.1 s, the total time of the $\gamma \rightarrow \alpha$ transformation is 0.5 s, which is twice as fast as the $\alpha \rightarrow \gamma$ transformation on heating. The results of profile analysis of this $\gamma(111)$ reflection are given in
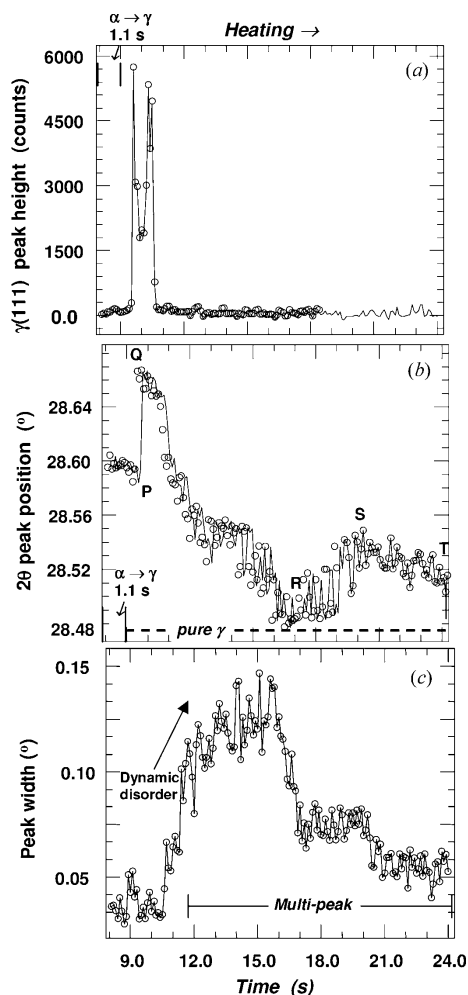
Figs. 10. On cooling from high temperatures immediately after the arc was turned off, the peak intensity (Fig. 10a) of this reflection exhibits a maximum value at $t = 25.6$ s, which indicates a gradual increase in texturing of the pure-γ microstructure in the negative temperature–time gradient. At $t = 25.6$ s, α-Fe appears, and the $\gamma \rightarrow \alpha$ transformation proceeds for the next 0.5 s, accompanied by a progressive drop in the $\gamma(111)$ intensity to zero on completion of the transformation. Within 0.2 s of power removal from the arc, the peak position (Fig. 10b) shows a monotonic increase in 2θ value, which indicates thermal contraction of the f.c.c. lattice on cooling to the end of the $\gamma \rightarrow \alpha$ transformation at $t = 26.1$ s. Interestingly, the peak width (Fig. 10c) increased immediately when the arc was turned off, attaining a maximum value at $t = 25.2$ s, and then decreased monotonically to the end of the transformation, which is indicative of reduced dynamic disorder as the system undergoes the $\gamma \rightarrow \alpha$ transformation on cooling. The $\gamma(200)$ reflection shows similar variations in peak intensity and peak position on cooling but has a shorter data range, as is evident in Fig. 9.

4.2.4. Back-transformed α-Fe on cooling. The frame-by-frame diffraction events from the start to the end of the $\gamma \rightarrow \alpha$ transformation on cooling are given in Fig. 11. When α-Fe first appears and
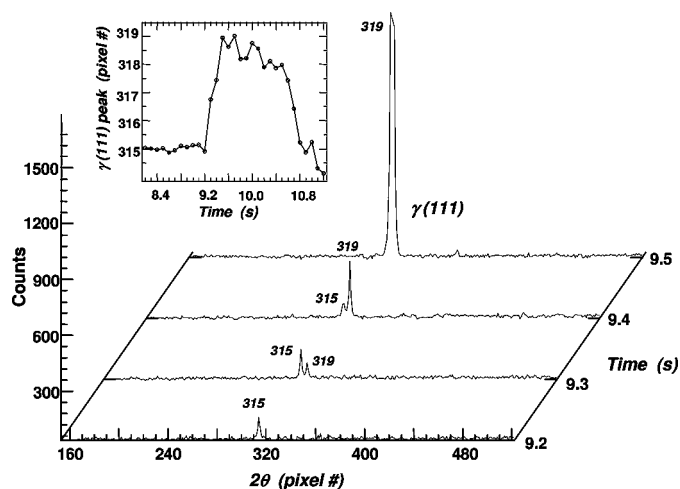

Figure 7
Profile analysis of the $\gamma(111)$ reflection shown in Fig. 6 as recorded in the HAZ on heating: (a) peak height, (b) peak position and (c) peak width (FWHM).

Figure 8
Frame-by-frame plot of the TRXRD patterns in an enlarged 2θ window of the $\gamma(111)$ reflection showing the experimental jump in peak position upon heating in the HAZ.
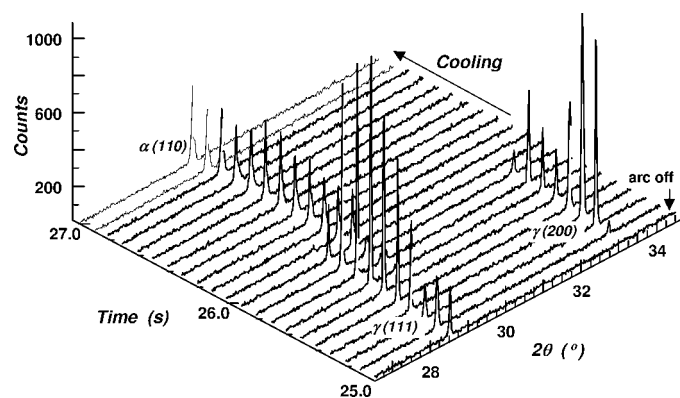

Figure 9
Frame-by-frame plot of the TRXRD patterns of the γ-Fe phase cooling in the HAZ, from the time of arc off to the end of the $\gamma \rightarrow \alpha$ transformation and beyond.

coexists with the transforming γ phase, the $\alpha(110)$ reflection is seen to be quite broad and exhibits a multiplet structure, which suggests that the newly back-transformed ferrite grains(domains) are very fine and/or disordered.

Within a few seconds of completion of the transformation, the ferrite grains and hence the overall microstructure attain a steady-state value as the steel weld cools. Profile analysis of the back-transformed $\alpha(110)$ reflection yields monotonic variations in the peak intensity, peak position and peak width. As seen in Fig. 12(a), the peak intensity is low at the start of the $\gamma \rightarrow \alpha$ transformation, increases steadily in the γ/α coexistence range and attains a steady value within ~8 s of the transformation. Similarly, as shown in Fig. 12(b), the peak position increases sharply in the first few seconds, which indicates thermal contraction on cooling, and climbs asymptotically to a steady value at $t = 34$ s. The peak width shown in Fig. 12(c) exhibits a large fluctuation at the start of the transformation, as seen in Fig. 11(b), but settles quickly to a low value, which indicates a monotonic decrease in thermal disorder on cooling.

Identical results are obtained for the $\alpha(211)$ reflection peak profile. Fig. 13 shows a plot of the FWHM of the $\alpha(211)$ peak in the same time regime as that for the $\alpha(110)$ peak shown in Fig. 12(c). Again, all the peak profiles for the back-transformed α-Fe were reproducible in three runs at the same location with a 540 µm pinhole at 50 ms time resolution.

4.3. Dynamics of phase transformation in the FZ

4.3.1. Annealing of α-Fe and $\alpha \rightarrow \gamma$ transformation on heating.
The TRXRD data shown in Fig. 2(a) for the phase transformation in the FZ at a location 3 mm away from the center of the liquid pool will now be examined in detail with profile analysis. Fig. 14(a) shows a

Figure 11
Frame-by-frame TRXRD plot at the start of the $\gamma \rightarrow \alpha$ transformation upon cooling in the HAZ, showing the first appearance of the (110) reflection of the back-transformed α-Fe. Each frame is 100 ms.
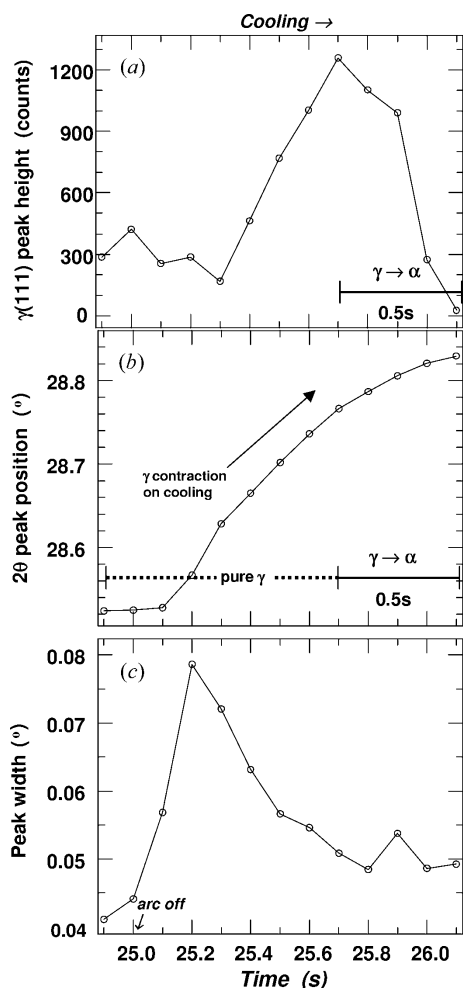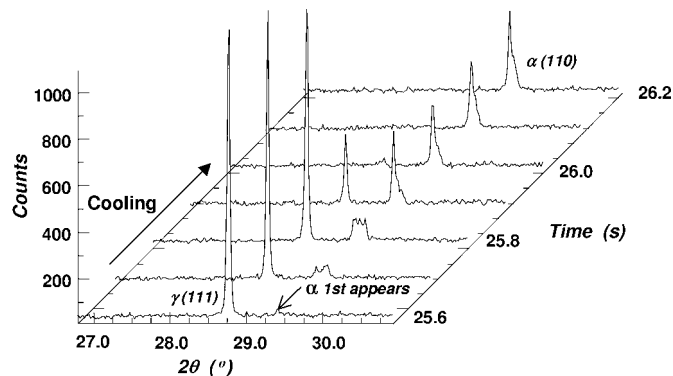

Figure 10
Profile analysis of the $\gamma(111)$ reflection shown in Fig. 9 as recorded in the HAZ on cooling: (a) peak height, (b) peak position and (c) peak width (FWHM).
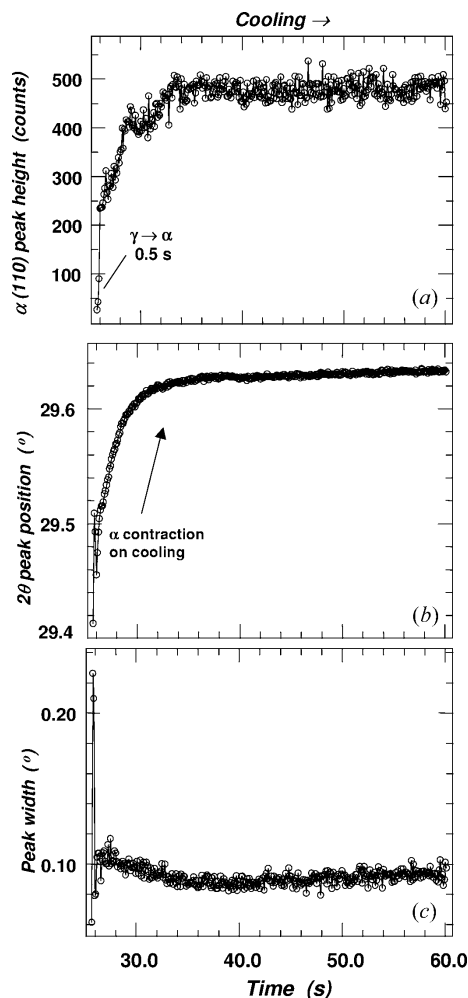

Figure 12
Profile analysis of the $\alpha(110)$ reflection shown in Fig. 11 as recorded in the HAZ on cooling: (a) peak height, (b) peak position and (c) peak width (FWHM).

pseudo three-dimensional frame-by-frame plot of the TRXRD patterns recorded in the first time segment associated with the heating of the base metal to the end of the $\alpha \rightarrow \gamma$ transformation from $t = 1.80$ s to $t = 3.60$ s. Annealing of the b.c.c. α phase took place initially for 1.30 s after the arc was turned on at $t = 1.20$ s. The $\alpha \rightarrow \gamma$ transformation began at $t = 2.50$ s, as shown by the first appearance of
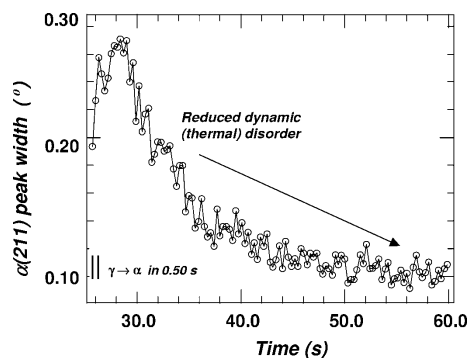
the γ phase, which is seen clearly in Fig. 14(b). At $t = 3.60$ s, α-Fe disappeared, indicating the completion of the $\alpha \rightarrow \gamma$ transformation. Again, according to the calculated phase diagram given in Fig. 3 and assuming no superheating, the temperatures at the start and end of this transformation should be 293 K and 1155 K. As can clearly be seen in Fig. 14(a), there are 23 frames of coexistence of the α and γ phases. Since the time resolution of each frame is 0.05 s, the total time for the $\alpha \rightarrow \gamma$ transformation is 1.15 s. Profile results for the $\alpha(110)$ peak height, peak position in 2θ and peak width (FWHM) on heating in the FZ are plotted in Fig. 15 as a function of time. These profiles are qualitatively similar to those of the $\alpha(110)$ reflection recorded in the HAZ (Fig. 5). During the initial heating in the first 2.5 s, the peak intensity is fairly constant. However, at the start of the $\alpha \rightarrow \gamma$ transformation, this reflection undergoes approximately a threefold fluctuation in peak intensity (Fig. 15a) and exhibits a multipeak feature that can be discerned clearly in Fig. 14(b). The increase in peak intensity and multiplet structure in the (110) reflection may be attributed to recrystallization of the base metal to yield a preferential (110) orientation of fine and relatively perfect grains in the microstructure at the start of the $\alpha \rightarrow \gamma$ transformation. The peak position initially decreases in 2θ value along the path PQ in Fig. 15(b), thus

Figure 13
FWHM of the $\alpha(211)$ reflection shown in Fig. 11 as recorded in the HAZ upon cooling, from the start of the $\gamma \rightarrow \alpha$ transformation to the end of the experimental run.
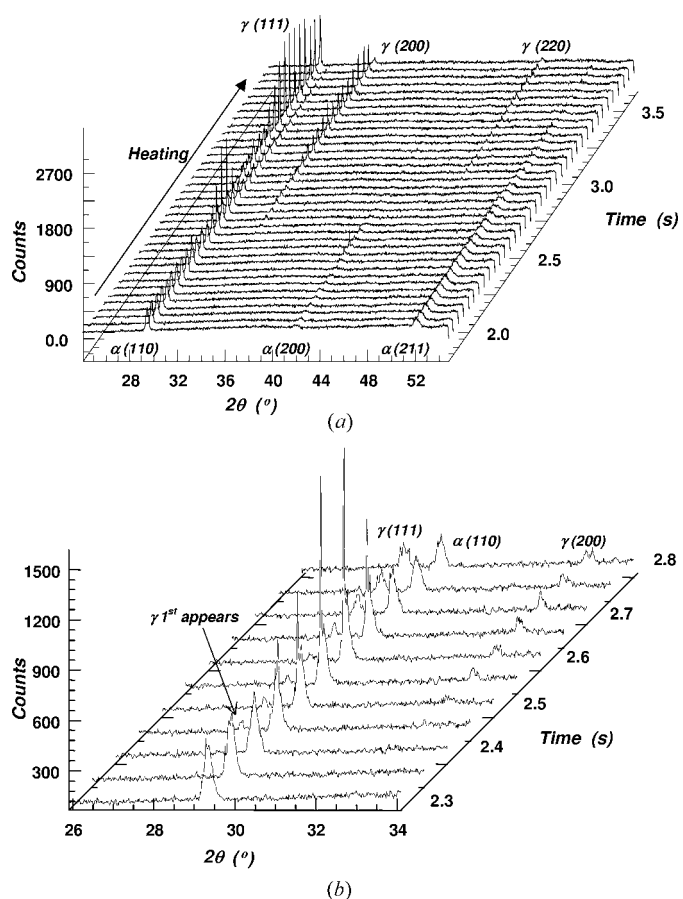

Figure 14
(a) Frame-by frame plot of the TRXRD patterns of the α-Fe and γ-Fe phases in the FZ on heating, from the time of arc on to the completion of the $\alpha \rightarrow \gamma$ transformation. (b) A zoom-in frame-by-frame plot of the TRXRD data showing the first appearance of the $\gamma(111)$ reflection at the start of the transformation. Each frame is 50 ms.
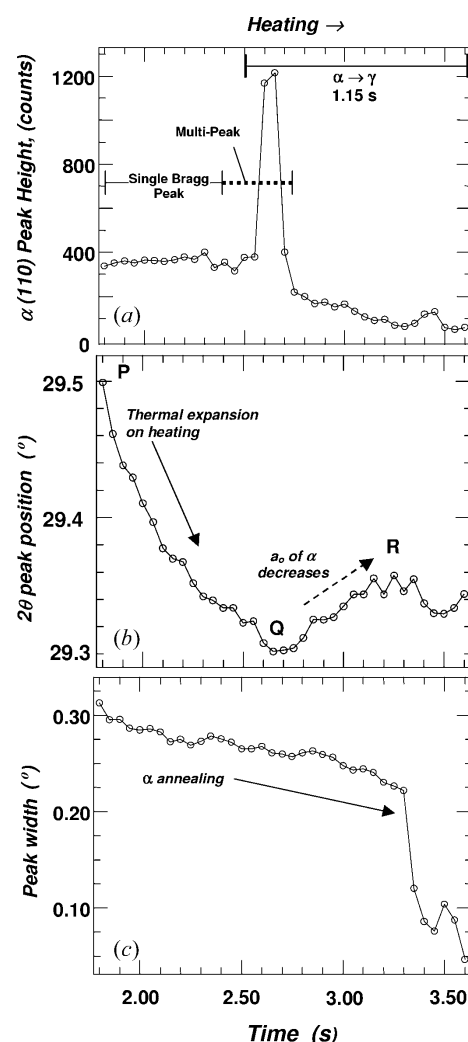

Figure 15
Profile analysis of the $\alpha(110)$ reflection shown in Fig. 14(a) as recorded in the FZ on heating: (a) peak height, (b) peak position and (c) peak width (FWHM).

indicating thermal expansion of the ferrite lattice with increasing temperature, in accordance with Bragg's law. Further heating along *QR* shows an increase in 2θ position similar to that observed in the HAZ (Fig. 5*b*); this increase corresponds to a decrease in (110)-spacing of the b.c.c. lattice. In contrast to the case in the HAZ, the decrease in the (110)-spacing of the ferrite base metal with continuing heating in the FZ occurs *during* the transformation instead of prior to it. In Fig. 15(*c*), the width of the $\alpha(110)$ reflection exhibits a monotonic decrease on heating from room temperature to well above the start of the transformation, which indicates thermal annealing and the relief of microstrain in the base metal with increasing temperature. Above $t = 3.30$ s, the peak width drops steeply before the α phase disappears at the end of the transformation.

4.3.2. γ-Fe during and after transformation on heating.

TRXRD patterns of the γ phase in the FZ on heating are shown in more detail in Fig. 16(*a*). The data cover the time regime from $t = 2.50$ s, at which γ-Fe first appeared, to $t = 10.50$ s, some 3 s before the steel melted. Profile analysis of the $\gamma(111)$ reflection is given in Fig. 17. The peak intensity of the $\gamma(111)$ reflection, plotted in Fig. 17(*a*), shows multiple fluctuations during the transformation and beyond, when γ-Fe exists as a pure phase in the microstructure. The intensity fluctuation in the period $t = 7.50$–10.50 s is associated with the appearance of a multipeak feature (Fig. 16*b*), which indicates multiple domain production in the pure-γ microstructure prior to melting. The peak position is given in Fig. 17(*b*) and shows an initial decrease along *QR* upon

transformation and a normal thermal expansion of the f.c.c. lattice with increasing temperature. With further heating along *RS*, the peak position shifts positively, implying an apparent decrease in cell parameter, similar to that found in the HAZ (Fig. 7*b*). Along *ST*, the γ phase once again undergoes normal thermal expansion with further temperature increases. The width of the $\gamma(111)$ reflection shown in Fig. 17(*c*) exhibits a peak in the transformation regime. This line broadening may be due to the formation of very fine and/or highly strained γ grains at the start of the transformation. With increasing temperature beyond $t \simeq 3.0$ s, annealing, recrystallization and grain growth give rise to the observed drop in width in both the single and the multipeak regime prior to melting.

4.3.3. The $\gamma \to \alpha$ transformation on cooling.

The arc was turned off at $t = 17.35$ s, and the liquid then cooled and solidified. The γ phase reappeared at $t = 17.50$ s and cooled and transformed as the temperature was lowered further. Fig. 18 shows a frame-by-frame plot of the TRXRD data in the time regime of the $\gamma \to \alpha$ transformation in the FZ on cooling. At $t = 18.10$ s, α-Fe first appeared, and at $t = 18.65$ s, all γ-Fe disappeared, marking the completion of the back transformation to the ferrite phase. As can be clearly seen in Fig. 18, there are 12 frames of coexistence of the γ and α phases. Since the time resolution of each frame is 0.05 s, the total time of the $\gamma \to \alpha$ transformation is 0.60 s. Like that in the HAZ, the $\gamma \to \alpha$ transfor-
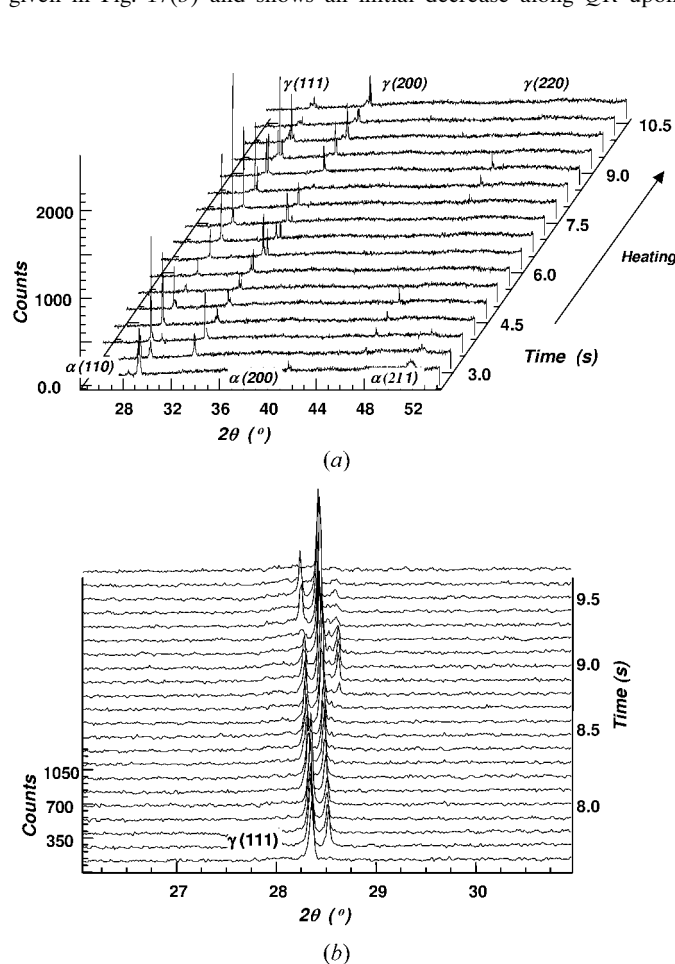

Figure 16
(*a*) TRXRD patterns of the γ-Fe phase in the FZ on heating, from the start of the $\alpha \to \gamma$ transformation to continued heating. For clarity, only every 10th of the 160 frames is plotted. (*b*) A zoom-in plot of the $\gamma(111)$ reflection showing the multipeak feature upon continued heating after the $\alpha \to \gamma$ transformation.
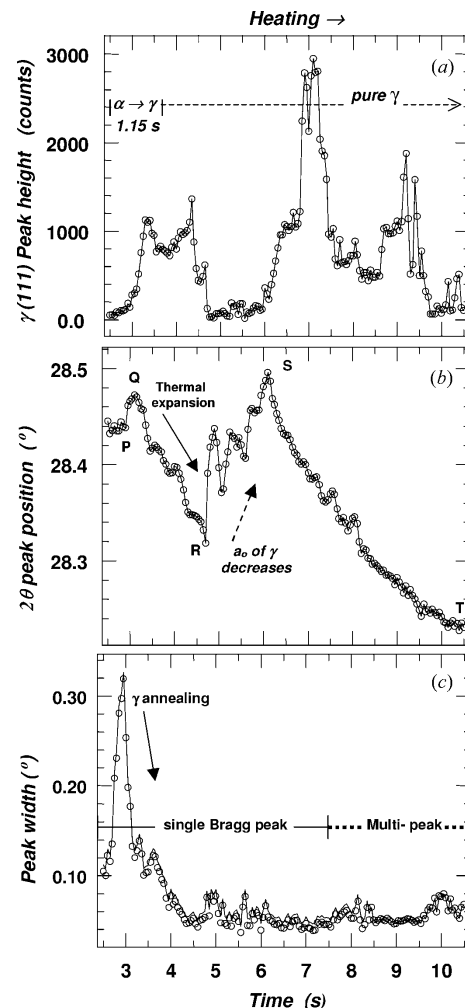

Figure 17
Profile analysis of the $\gamma(111)$ reflection shown in Fig. 16 as recorded in the FZ on heating: (*a*) peak height, (*b*) peak position and (*c*) peak width (FWHM).

mation on cooling in the FZ is about twice as fast as the $\alpha \rightarrow \gamma$ transformation on heating. However, note that, in the FZ, the solidified γ phase exhibits a (200) texture, as shown by a preference of the (200) reflection over the (111) reflection. This preferential (200) texturing is reproducible in four independent TRXRD experiments using various combinations of pinhole size (260, 730 µm), time resolution (50, 100, 200 ms) and X-ray energy (7.0, 9.6, 12.0 keV).

The results of profile analysis of the γ(200) reflection from the FZ are given in Fig. 19. Upon solidification, immediately after the arc was turned off, and cooling from high temperatures, the peak intensity (Fig. 19a) of this reflection exhibits a maximum at $t = 17.65$ s, which implies an initial increase followed by a more gradual decrease in texturing of the pure-γ microstructure on cooling. At $t = 18.10$ s, α-Fe appears, and the $\gamma \rightarrow \alpha$ transformation proceeds in the next 0.60 s, accompanied by a further drop in the γ(200) intensity to zero upon completion of the transformation. The peak position, however, shows a monotonic increase in 2θ value (Fig. 19b), which implies a normal thermal contraction of the f.c.c. lattice with cooling until the end of the $\gamma \rightarrow \alpha$ transformation at $t = 18.65$ s. Interestingly, the peak width (Fig. 19c) exhibits a gentle increase initially upon cooling in the pure-γ microstructure and undergoes a further twofold increase during the $\gamma \rightarrow \alpha$ transformation. The monotonic increase in diffraction peak width with decreasing temperature can only be due to the net effect of increased strain over that of reduced thermal disorder on cooling and domain production during the transformation process. The γ(111) reflection shows similar variations in peak intensity, peak position and peak width on cooling but has a lower signal-to-noise level, as is evident in the TRXRD data shown in Fig. 18.

4.3.4. Back transformed α-Fe on cooling. Fig. 20 shows a pseudo three-dimensional plot of the TRXRD patterns from $t = 18.10$ s, when α-Fe was first back transformed from the γ phase in the FZ upon cooling, to $t = 30.00$ s, at the end of the diffraction run. Again, for clarity, only every seventh of the 238 diffraction patterns is plotted. The frame-by-frame diffraction events from the start to the end of the $\gamma \rightarrow \alpha$ transformation were described in §4.3.3 and plotted in Fig. 18.

The results of the profile analysis of the α(110) reflection of the back-transformed ferrite phase are shown in Fig. 21. As seen in Fig. 21(a), the peak intensity is low at the start of the $\gamma \rightarrow \alpha$ transformation, increases rapidly in the γ/α coexistence regime, attaining a

maximum value at the completion of the transformation, and decreases continuously thereafter as the all-α microstructure in the FZ is cooled. In Fig. 21(b), the peak position is seen to increase sharply in the first 3 s or so, which indicates thermal contraction on cooling, and climbs asymptotically to a steady value at $t \simeq 25$ s. The
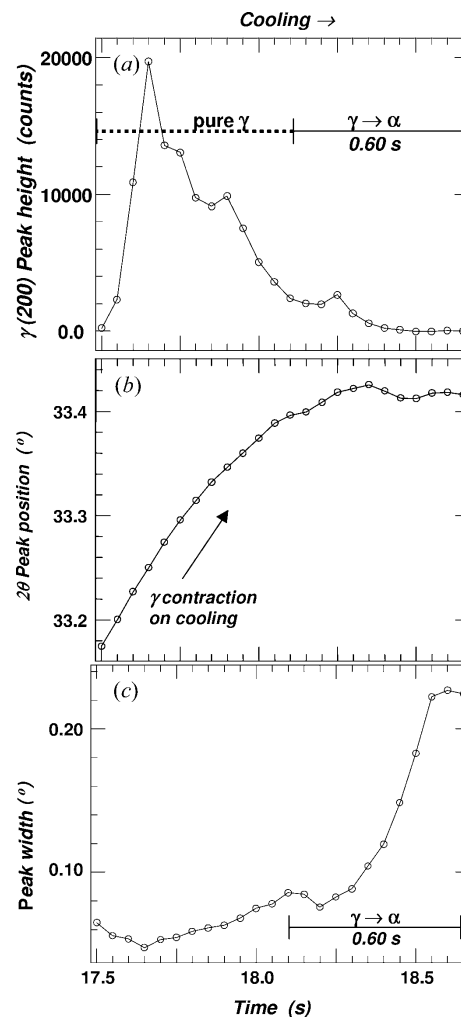

Figure 19
Profile analysis of the γ(200) reflection shown in Fig. 18 as recorded in the FZ on cooling: (a) peak height, (b) peak position and (c) peak width (FWHM).
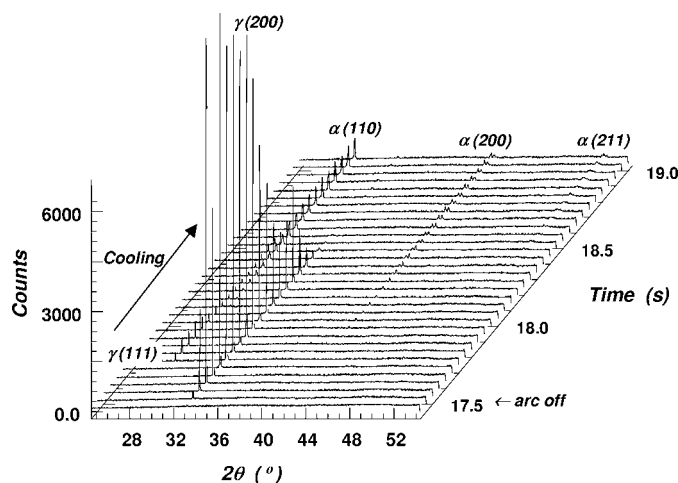

Figure 18
Frame-by-frame plot of the TRXRD patterns of the γ-Fe phase, showing a preferential (200)-texture upon cooling in the FZ, from the time of arc off to the end of the $\gamma \rightarrow \alpha$ transformation and beyond. Each frame is 50 ms.
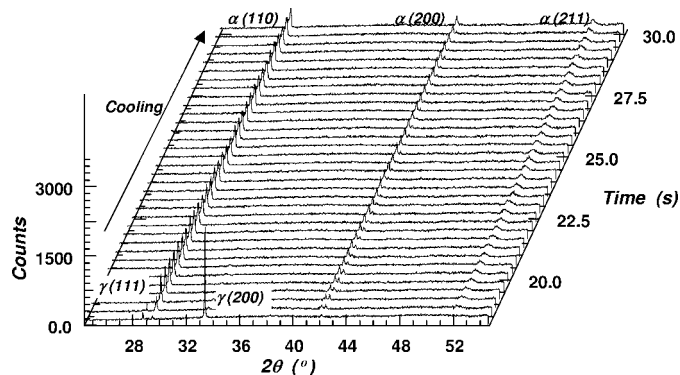

Figure 20
TRXRD patterns of back-transformed α-Fe in the FZ on cooling, from the start of the $\gamma \rightarrow \alpha$ transformation to the end of the experimental run. For clarity, only every seventh of the 250 frames is plotted.

peak width shown in Fig. 21(c) exhibits an initial jump in the $\gamma \to \alpha$ transformation range and continues to increase, but at a lower rate, as the weld cooled. This behavior in the FZ is contrasted with that in the HAZ, in which the width of the back-transformed $\alpha(110)$ reflection shows an expected decrease to a constant low value (Fig. 12c), with reduced thermal disorder on cooling.

Careful examination reveals the development of a shoulder on the low-2θ side of the $\alpha(110)$ reflection on cooling in the FZ. This shoulder feature can be seen clearly in an enlarged view of the time-resolved $\alpha(110)$ reflection plotted in Fig. 22. The inset in Fig. 22 is a deconvolution of the last TRXRD frame and reveals unambiguously the existence of the shoulder feature in this reflection. A more detailed frame-by-frame profile analysis shows that each of the components in the doublet shift in opposite directions on cooling, thus resulting in an increase in the overall width of the $\alpha(110)$ reflection. Furthermore, to check the reproducibility of this feature in the FZ, we performed additional TRXRD measurements. We enhanced the angular resolution in 2θ and the spatial resolution on the sample by lowering the photon energy from 12 to 7 keV (0.17711 nm) and reducing the pinhole from 730 to 260 µm, respectively. These results are plotted in Fig. 23 and indeed show a well resolved doublet feature in the $\alpha(110)$ reflection upon cooling in the FZ. This doublet feature is highly reproducible (ten times) with other combinations of photon energy, pinhole size and time resolution.
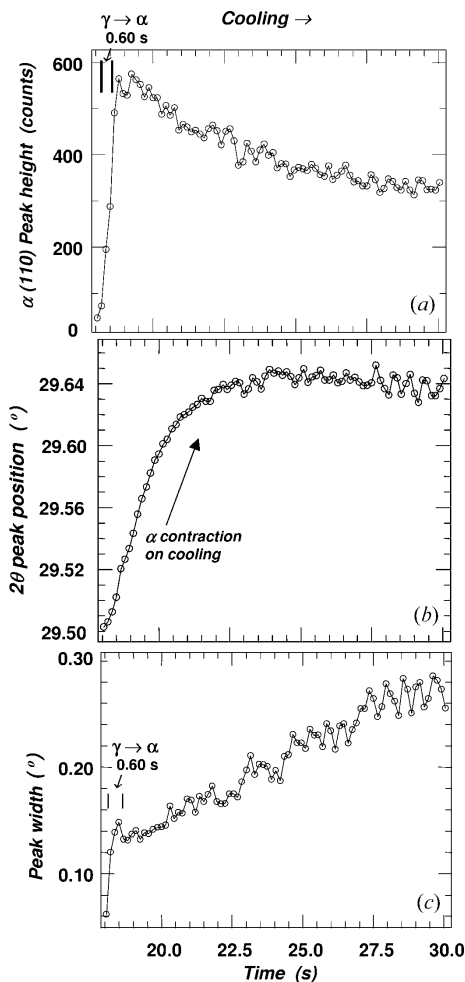
Table 1
Calculated 2θ splitting of the (110) and (101) reflections in Fe–C martensite as a function of carbon content and photon energies, and a comparison with experimental values.

wt% carbon	$2\theta_{110}$–$2\theta_{101}$ splitting (°)	
	At 12 keV	At 7 keV
0.05	0.034	0.063
0.25	0.168	0.309
0.50	0.264	0.486
Experimental	0.16	0.37

The observed doublet in the $\alpha(110)$ reflection may arise from (i) the existence of b.c.c. α-Fe in two morphological forms in the FZ microstructure or (ii) the formation of a body-centered tetragonal (b.c.t.) Fe–C martensite in the FZ, which is undergoing a much higher cooling rate than the HAZ. It is well known that, at a high quenching rate, f.c.c. Fe–C alloys may transform to a b.c.t. martensite (Honeycomb, 1982; Cohen, 1962), giving rise to splittings in various reflections in the diffraction pattern as a result of the induced tetragonality in the structure. The splitting can be calculated, since the a and c parameters of the martensite phase are known experimentally as a function of their carbon contents (Roberts, 1953),

$$a = 2.86678 - 0.013 \times \text{wt\% C}, \qquad (2)$$

$$c = 2.86678 + 0.116 \times \text{wt\% C}. \qquad (3)$$

Thus, using the *PowderCell* code and known crystallographic parameters for the b.c.t. Fe–C martensite (Petch, 1943), the splitting of the $\alpha(110)$ reflection into b.c.t.(101) and b.c.t.(110) reflections has been calculated for various carbon contents in the Fe–C martensite phase at two photon energies (wavelengths): 12 and 7 keV. The results are given in Table 1, together with the experimental observed splitting of 0.16° at 12 keV (Fig. 22) and 0.37° at 7 keV (Fig. 23). From Table 1, it
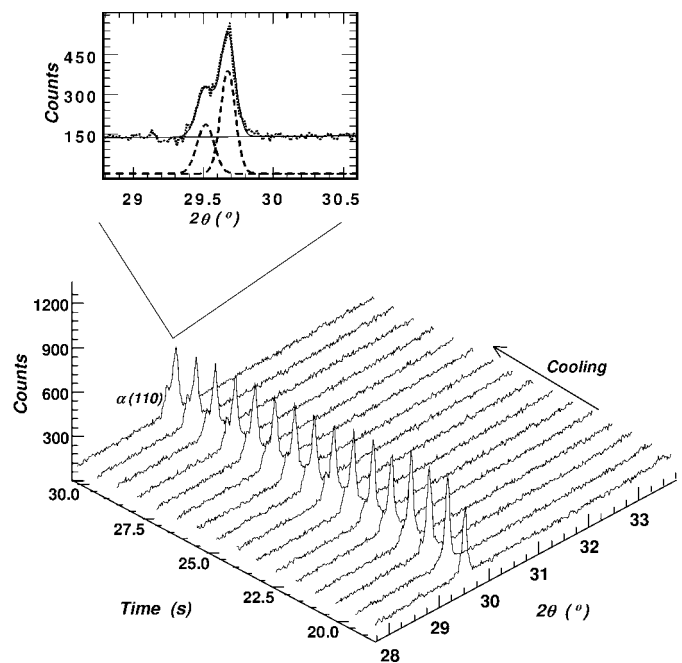

Figure 21
Profile analysis of the $\alpha(110)$ reflection shown in Fig. 19 as recorded in the FZ on cooling: (a) peak height, (b) peak position and (c) peak width (FWHM).

Figure 22
Zoom-in TRXRD plot in the 2θ window of the $\alpha(110)$ reflection showing the development of a shoulder feature on cooling. For clarity, every 15th of the 250 frames is plotted. The inset is a deconvolution of the shoulder feature at the last frame using a two-Gaussian fit.

is seen that the splitting of the b.c.t.(110) and b.c.t.(101) reflections systematically increases with carbon content because of an increase in tetragonal distortion with carbon concentration in the martensite structure. At 0.05 wt% C, which is the bulk carbon content in the steel currently studied (see §2), the expected splitting is only 0.034° at 12 keV, which is much smaller than the observed value of 0.16°. The latter would correspond to the splitting of an Fe–C martensite containing 0.25 wt% C. Similarly, at 7 keV, the observed 0.37° splitting is again much larger than that for the carbon content of our steel system. Thus it is unlikely that the observed doublet in the α(110) reflection is due to the formation of an Fe–C martensite. It is likely, therefore, that the microstructure in the FZ contains b.c.c. α-Fe as a single crystallographic phase, but that this phase coexists in two morphological entities, such as allotriomorphic ferrite and Widmanstatten ferrite (Zhang *et al.*, 2002*a*), each having a slightly different b.c.c. lattice parameter.

4.3.5. The δ-Fe phase. The occurrence of the b.c.c. δ-Fe phase at high temperature has only been detected in one out of the 15 TRXRD experimental runs in the FZ of the C–Mn steel weld. Selected diffraction frames obtained at a location 2 mm from the weld center using a 260 μm pinhole and 200 ms time resolution at 7 keV are shown in Fig. 24. The weld melts at $t = 1.0$ s, producing no Bragg reflection in the TRXRD pattern. The arc was turned off at $t = 2.4$ s, and in the next frame, at $t = 2.6$ s, the δ(110) reflection was recorded and shown to be already in coexistence with the γ(111) reflection. Subsequent frames at $t = 4.2$, 5.8 and 7.6 s show the growth of the γ phase and the $\alpha \rightarrow \gamma$ transformation all the way to pure back-transformed α-ferrite. The δ(110) peak has a relatively low intensity but occurs at a distinct 2θ value and in a different sequence of events from that of the α(110) reflection. Similarly, infrequent detection of the δ phase has also been noted in moving weld experiments of the same material reported recently (Elmer *et al.*, 2001). This result may be due to a combination of the narrowness of the δ phase field (Fig. 3) and the fast kinetics of the $\delta - \gamma$ transformation at high temperatures.

5. Summary and concluding remarks

We have applied a refined version of our time-resolved diffraction technique (Wong *et al.*, 1990; Larson *et al.*, 1993) using an intense synchrotron beam emitted from a multipole wiggler at Stanford Synchrotron Radiation Laboratory and performed a detailed investigation to follow crystallographically solid-state phase transforma-
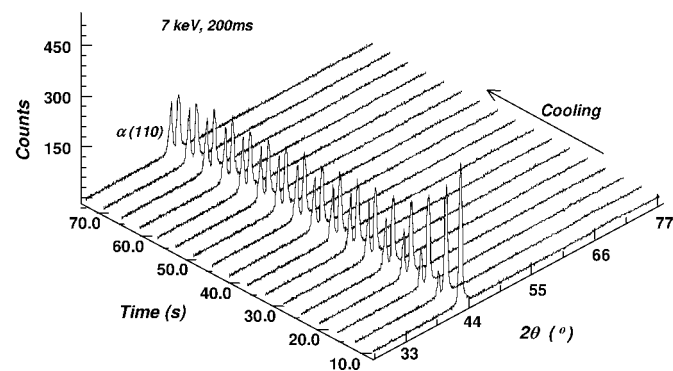
tions in a highly non-isothermal system. Our findings in the heat-affected and fusion zones of a C–Mn steel spot weld may be summarized as follows:

(i) The $\alpha \rightarrow \gamma$ transformation times on heating in both the HAZ and the FZ are very similar, being 1.1 s and 1.15 s, respectively, but are twice as long as those of the $\gamma \rightarrow \alpha$ transformation on cooling in both cases, being 0.5 s and 0.60 s, respectively. The transient 'spot' welds studied in this investigation heat and cool at much higher rates than conventional moving welds, hence the experimental measurement of temperatures is extremely difficult. For example, thermocouple plunge experiments performed in a similar steel alloy (Babu *et al.*, 2002) indicate that the cooling rates under these conditions can exceed 1000 K s^{-1}, and these experiments cannot be performed *in situ* during the TRXRD experiment. Since the kinetic analysis of the TRXRD data will require a knowledge of thermal cycles at various locations in the weldment, a practical recourse is to use numerical heat-transfer and fluid-flow modeling to obtain accurate transient temperature fields, peak temperatures, and heating and cooling rates at all locations of the weldment. Such a model is being developed in collaboration with the Pennsylvania State University, and preliminary results are presented in Fig. 25. This figure shows the time–temperature profiles of four different locations with respect to the center of the weld. Clearly, in these spot weld experiments the weld heats more slowly than it cools, as expected. This difference in heating and cooling rates is most likely why the transformation time is shorter on cooling than on heating. More detailed and more systematic modeling needs to be carried out in this area to correlate the calculated temperature profiles to the TRXRD results.

(ii) Systematic and detailed profile analyses of the TRXRD patterns show that in both the HAZ and the FZ, in addition to the expected thermal annealing and thermal expansion on heating, there are intricate processes that cause an apparent decrease in the (110) d-spacing of the α-ferrite phase prior to (in the HAZ) or during (in the FZ) the $\alpha \rightarrow \gamma$ transformation on heating (Figs. 5*c* and 15*c*). A similar decrease in the (111) d-spacing of the γ-austenite phase (Figs. 7*c* and 17*c*) after the $\alpha \rightarrow \gamma$ transformation with *increasing* temperature was also observed. This apparent *decrease in d-spacing with increased temperature* is probably due to carbide precipitation and/or tensile stress relief in the case of α-Fe, and stress relief in γ-Fe
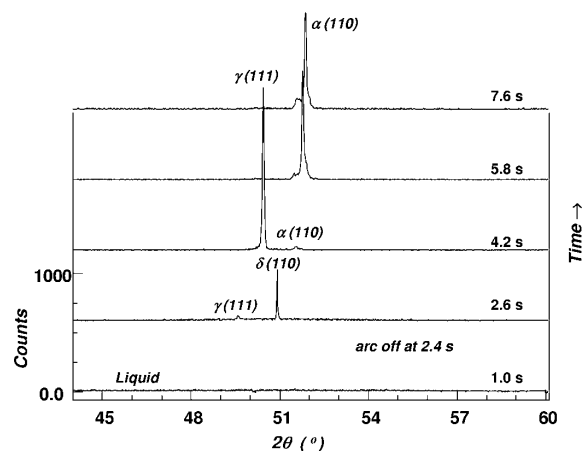

Figure 23
Zoom-in TRXRD plot in the 2θ window of the α(110) reflection showing a well resolved doublet feature; from a control experimental run in the FZ using a 7 keV photon beam and a 260 μm pinhole with a 200 ms time resolution. For clarity, every 20th of the 340 frames is plotted.

Figure 24
Detection of δ-Fe in the FZ at a location 2 mm from the center of the weld. The TRXRD patterns were recorded using a 7 keV (0.1771 nm) photon beam, 260 μm pinhole and a time resolution of 200 ms.
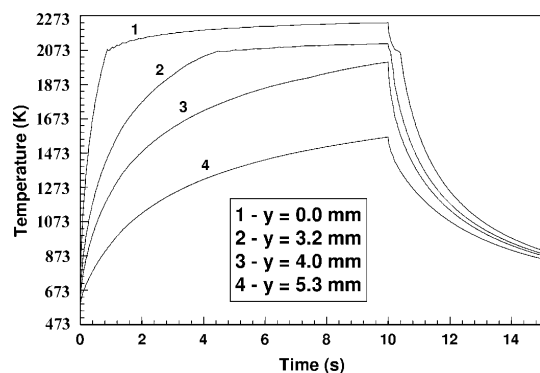
Figure 25
Weld thermal cycles at different monitoring locations. The *y* values indicate the distance from the weld center line (Zhang *et al.*, 2002*b*).

resulted in a phase transformation from a lower-density (b.c.c. at 7.789 gm cc^{-1}) to a slightly higher-density (f.c.c. at 7.862 gm cc^{-1}) phase.

(iii) Microstructural differences, however, exist between the HAZ and the FZ. In particular:

(*a*) In the FZ, the back-transformed γ-Fe on solidification of the liquid has a strong (200) texture (Fig. 18), whereas, on cooling in the HAZ, the γ-Fe retains largely the (111) texture (Fig. 9) induced in the $\alpha \rightarrow \gamma$ transformation on heating.

(*b*) In the HAZ on cooling, the width of the γ(111) reflection increases initially, which indicates strain in the microstructure, but decreases as expected with the reduction of dynamic disorder with further cooling (Fig. 10*c*) until the end of the $\gamma \rightarrow \alpha$ transformation. In the FZ, however (Fig. 19*c*), the strain in the γ phase increases steadily on solidification and exhibits a jump in the entire period of the $\gamma \rightarrow \alpha$ transformation on further cooling.

(*c*) In the FZ, the final microstructure is likely to consist of a single α phase dispersed in two morphological entities (Fig. 26*b*), whereas, in the HAZ, the α phase persists in one morphological entity in the final microstructure (Fig. 26*a*).

(iv) Finally, the δ phase crystallizing from the liquid in the FZ remains rather elusive, being detected only in one out of the 15 attempted TRXRD experiments.

In conclusion, the work reported here for a C–Mn steel fusion weld clearly illustrates the novelty and usefulness of time-resolved diffraction with intense synchrotron radiation for the purpose of following (i) solid-state transformations crystallographically and (ii) microstructure evolution with submillimeter spatial resolution during materials processing at high temperature and with time resolution down to 50 ms. Key to the dynamics of high-temperature systems is the temperature–time relationship, which, for the case of a highly non-isothermal system, is not easily attainable experimentally by contact (thermocouples) or non-contact means (pyrometry) (Farson *et al.*, 1998). Recourse has to be sought in modeling to obtain such temperature–time relationships, in order to render a more complete picture of the material dynamics in the non-isothermal processes exemplified by the fusion welds presented here.
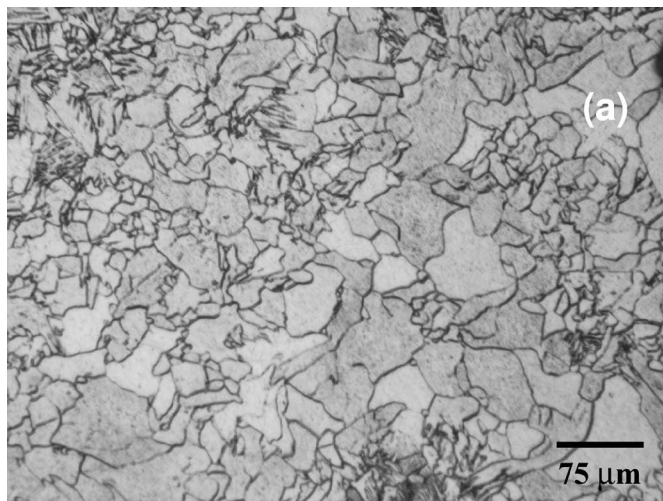
Figure 26
Optical micrographs showing the final microstructure at completion of each of the TRXRD experiments (*a*) in the HAZ and (*b*) in the FZ. The latter clearly shows two distinct morphological regions.

References

Ashby, M. F. & Easterling, K. E. (1982). *Acta Metall.* **30**, 1969–1980.
Babu, S. (2000). Personal communication.
Babu, S. S., Elmer, J. W., David, S. A. & Quintana, M. (2002). *Proc. R. Soc. Ser. A*, **458**, 811–821.
Bearden, J. A. & Burr, A. F. (1967). *Rev. Mod. Phys.* **39**, 125–137.
Cohen, M. (1962). *Trans. AIME*, **224**, 638–665.
Easterling, K. (1983). *Introduction to the Physical Metallurgy of Welding*, ch. 3. London: Butterworths.
Elmer, J. W., Wong, J., Fröba, M., Waide, P. A. & Larson, E. M. (1996). *Metall. Mater. Trans. A*, **27**, 775–783.
Elmer, J. W., Wong, J. & Ressler, T. (1998). *Metall. Mater. Trans. A*, **29**, 2761–2773.
Elmer, J. W., Wong, J. & Ressler, T. (2000). *Scr. Mater.* **43**, 751–757.
Elmer, J. W., Wong, J. & Ressler, T. (2001). *Metall. Mater. Trans. A*, **32**, 1175–1187.

Farson, D., Richardson, R. & Li, X. (1998). *Welding J.* **77**, 396s–401s.

Grong, Ø. (1994). *Metallurgical Modelling of Welding*, ch. 1. London: Institute of Materials.

Harrison, P. L. & Farrar, R. A. (1989). *Int. Mater. Rev.* **34**, 35.

Honeycomb, R. W. K. (1982). *Steels, Microstructure and Properties*, ch. 1. Materials Park, OH: ASM.

Ion, J. C., Easterling, K. E. & Ashby, M. F. (1984). *Acta Metall.* **32**, 1949.

Karpenko, V., Kinney, J. H., Kulkarni, S., Neufeld, K., Poppe, C., Tirsell, K. G., Wong, J., Cerino, J., Troxel, T., Yang, J., Hoyer, E., Green, M., Humpries, D., Marks, S. & Plate, D. (1989). *Rev. Sci. Instrum.* **60**, 1451–1460.

Larson, E. M., Wong, J., Holt, J. B., Waide, P., Rupp, B. & Terminello, L. (1993). *J. Mater. Res.* **8**, 1533–1541.

Mundra, K., DebRoy, T., Babu, S. S. & David, S. A. (1997). *Welding J.* **76**, 163s–172s.

Palmer, T. A., Elmer, J. W. & Wong, J. (2001). *Sci. Tech. Welding Joining*, **7**(3), 159–171.

Petch, N. J. (1943). *J. Iron Steels Inst.* **147**, 221.

Ressler, T. (1997). *J. Phys IV*, **7**, 269–272.

Ressler, T., Wong, J. & Elmer, J. W. (1998). *J. Phys. Chem.* B**102**, 10724–10735.

Roberts, C. S. (1953). *Trans. AIME*, **197**, 203–215.

ST121 Detector & Controller Manual (1996). *Princeton Instruments Reviews B.* 3660 Quakerbridge Road, Trenton, NJ 08619, USA.

Sundman, B., Jansson, B. & Andersson, J. (1985). *Calphad*, **9**, 153–170.

Vander Voort, G. F. (1991). *Atlas of Time–Temperature Diagrams for Irons and Steels.* Cleveland, OH: ASM International.

Wong, J., Elmer, J., Waide, P. & Larson, E. M. (1994). *Adv. X-ray Anal.* **37**, 479–485.

Wong, J., Fröba, M., Elmer, J. W., Waide, P. A. & Larson, E. J. (1997). *Mater. Sci.* **32**, 1493–1500.

Wong, J., Larson, E., Holt, J., Waide, P., Rupp, B. & Frahm, R. (1990). *Science*, **249**, 1906–1909.

Wychoff, R. W. G. (1963). *Crystal Structure*, Vol. 1, p. 16. New York: John Wiley and Son.

Yang, Z. & DebRoy, T. (1997). *Sci. Technol. Welding Joining*, **2**, 1–6.

Yang, Z. & DebRoy, T. (1999). *Metall. Mater. Trans. B*, **30**, 483–489.

Yang, Z., Elmer, J. W., Wong, J. & DebRoy, T. (2000). *Welding J.* **79**, 97s–112s.

Zhang, W., Elmer, J. W. & DebRoy, T. (2002a). *Mater. Sci. Eng.* **333**, 321–335.

Zhang, W., Elmer, J. W. & DebRoy, T. (2002b). Personal communication.

 167